Physical Properties of Annealed ZnO Nanowire/CuSCN Heterojunctions for Self-Powered UV Photodetectors

Jérôme Garnier,*[†,‡] Romain Parize,[†,‡] Estelle Appert,[†,‡] Odette Chaix-Pluchery,[†,‡] Anne Kaminski-Cachopo,[§,‖] and Vincent Consonni[†,‡]

[†]Univ. Grenoble Alpes, LMGP, F-38000 Grenoble, France
[‡]CNRS, LMGP, F-38000 Grenoble, France
[§]Univ. Grenoble Alpes, IMEP-LAHC, F-38000 Grenoble, France
[‖]CNRS, IMEP-LAHC, F-38000 Grenoble, France

S *Supporting Information*

ABSTRACT: The low-cost fabrication of ZnO nanowire/CuSCN heterojunctions is demonstrated by combining chemical bath deposition with impregnation techniques. The ZnO nanowire arrays are completely filled by the CuSCN layer from their bottoms to their tops. The CuSCN layer is formed of columnar grains that are strongly oriented along the [003] direction owing to the polymeric form of the β-rhombohedral crystalline phase. Importantly, an annealing step is found essential in a fairly narrow range of low temperatures, not only for outgassing the solvent from the CuSCN layer, but also for reducing the density of interfacial defects. The resulting electrical properties of annealed ZnO nanowire/CuSCN heterojunctions are strongly improved: a maximum rectification ratio of 2644 at ± 2 V is achieved following annealing at 150 °C under air atmosphere, which is related to a strong decrease in the reverse current density. Interestingly, the corresponding self-powered UV photodetectors exhibit a responsivity of 0.02 A/W at zero bias and at 370 nm with a UV-to-visible (370−500 nm) rejection ratio of 100 under an irradiance of 100 mW/cm^2. The UV selectivity at 370 nm can also be readily modulated by tuning the length of ZnO nanowires. Eventually, a significant photovoltaic effect is revealed for this type of heterojunctions, leading to an open circuit voltage of 37 mV and a short circuit current density of 51 μA/cm^2, which may be useful for the self-powering of the complete device. These findings show the underlying physical mechanisms at work in ZnO nanowire/CuSCN heterojunctions and reveal their high potential as self-powered UV photodetectors.

KEYWORDS: *copper thiocyanate, zinc oxide nanowires, self-powered UV photodetectors*
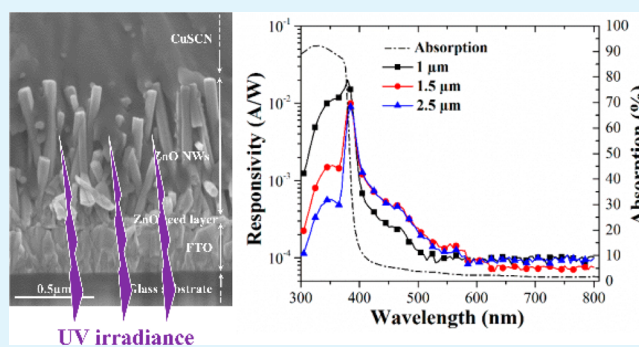
1. INTRODUCTION

Over the past decades, zinc oxide (ZnO) has received a large interest owing to its wide band gap energy of 3.3 eV at room temperature, its high exciton binding energy of 60 meV, and its high electron mobility.[1] Moreover, ZnO offers the possibility to form nanowires (NWs) by a wide number of physical and chemical deposition techniques[2] such as physical vapor deposition,[3] thermal evaporation,[4] pulsed laser deposition,[5] electrodeposition,[6] or chemical bath deposition.[7−11] The growth in solution benefits from the low growth temperature, low cost and easiness to scale-up. However, a ZnO seed layer is required to control the growth of ZnO NWs in solution. The structural properties of ZnO NWs strongly depend on the structural morphology of the ZnO seed layer, such as nanoparticle size, density, orientation, polarity, and porosity.[12,13] The growth conditions in the chemical bath such as the nature of chemical precursors and related concentrations, pH,

and additives are also crucial for controlling the structural morphology of ZnO NWs.[7−11]

Owing to the expected increase in light harvesting[14] and extraction efficiency, as well as charge carrier management, the integration of ZnO NWs has recently been achieved in optoelectronic and photovoltaic devices such as light emitting diodes[15] and nanostructured solar cells.[16,17] In the case of nanostructured solar cells, a hole transporting materials (HTM) is required, especially in dye-sensitized solar cells (DSSCs),[16,18] extremely thin absorber (ETA),[17] and quantum dot-sensitized solar cells (QDSCs)[19] and should ensure a good pore-filling. Electrolytes with iodide/tri-iodide redox couple have typically been used for DSSCs, but new promising possibilities of p-type semiconductors such as CuAlO$_2$,[20] NiO,[21] CuI[22] or copper

thiocyanate (CuSCN)[23] have further been considered for all-inorganic solar cells. Among them, CuSCN is an inorganic p-type semiconductor with a wide band gap energy in the range of 3.6−3.9 eV,[24,25] exhibiting high transparency in the visible range but a relatively low hole conductivity of 0.01 S m^{-1}.[26] The enhancement of the hole conductivity can be achieved through the formation of Cu vacancies (V_{Cu})[27] or through the doping of the solution with $(SCN)_2$ groups.[25] In this way, a maximum hole conductivity of 1.42 S m^{-1} has already been reported for the structurally modified CuSCN layer.[26] CuSCN is also a promising HTM because it can be easily grown by electrodeposition,[28] successive ionic layer adsorption and reaction techniques,[29] or impregnation techniques.[23] These assets have led to the incorporation of CuSCN into new optoelectronic devices,[30−35] including thin film transistors (TFT)[36] and self-powered UV photodetectors for instance.[37,38]

The self-powered UV photodetectors involving wide band gap semiconductors have recently attracted much attention. They can either be integrated with an energy harvester unit, such as piezoelectric nanogenerators or solar cells, be coupled with an energy storage unit to power them or, more interestingly, be self-sufficient and independent upon external power sources by benefiting from their photovoltaic behavior.[38] The latter configuration used as a p-n photodiode does not need constant external bias voltage and thus may reduce energy consumption. This is in contrast to standard ZnO NW-based UV photodetectors integrating Schottky metal−semiconductor diodes, for which oxygen adsorption/desorption mechanisms are involved, generally working at relatively high bias voltage in order to prevent electron−hole pair recombinations and to favor the detectability of the UV signal.[39−42] The high responsivity above 10^2 A/W is typically achieved in these standard UV photodetectors, but at the expense of the external bias used, that is hardly compatible with self-powered multifunctional nanodevices. Interestingly, higher sensitivity, faster response times, and no oxygen dependency are expected for the self-powered UV photodetectors. Additionally, the use of ZnO NWs is essential to increase the active surface area and enhance photovoltaic and responsivity effects. Several combinations of semiconductors have already been used in self-powered UV photodetectors such as NiO/ZnO core−shell NW heterojunctions (responsivity $R_{365\ nm}$ = 0.493 mA/W under xenon lamp),[43] TiO$_2$/iodide electrolyte similar to DSSCs[44] (short circuit current I_{sc} = 2.5 µA at 330 nm under light intensity of 20 mW/cm^2), TiO$_2$/ZnO nanostructures[45] ($R_{365\ nm}$ = 0.4 A/W under light intensity of 50 µW/cm^2), or ZnO/Pt Schottky-type heterojunctions[46] (I_{sc} = 47.5 nA at 365 nm under light intensity of 0.47 mW/cm^2). ZnO NW/CuSCN heterojunction is a very recent device that has shown great potential: CuSCN is directly used as a p-type semiconductor associated in a p-n heterojunction with n-type ZnO NW arrays. The present heterojunction has already shown a good rectifier behavior: the rectification ratio (RR) comparing the currents at forward and reverse voltages has been reported in the ranges of 1−10^2[30−32] for electrodeposited CuSCN and of 10^2−10^3 for impregnated CuSCN at ±2 V.[33] Recently, the heterojunction prepared with CuSCN deposited by spray technique associated with air heat treatment of ZnO NW arrays have even reached a RR of 21 500.[34] Eventually, a responsivity of 0.0075 A/W at 355 nm for 6 mW cm^{-2} irradiance and a minimum UV-to-visible rejection ratio of about 100 has been determined for self-powered UV photodetectors based on ZnO NW/CuSCN heterojunctions, but with a low RR of 23 at ±4 V drastically

limiting their photovoltaic effect (V_{OC} = 1 mV, I_{SC} < 20 µA).[37] That low photovoltaic effect may be the sign of a relatively poor interface quality, requiring the development of postgrowth treatment. For instance, the solvent outgassing from the CuSCN layer is well-known to improve its structural and electro-optical properties:[55,56] a 5 × 10^{-2} mbar vacuum treatment for 2 h or a storage under nitrogen atmosphere for several days have been shown to improve the photovoltaic performances of TiO$_2$/Dye/CuSCN solar cells through a continued slow solvent outgassing.[55] Similarly, the short-circuit current density has been increased to 2 mA/cm^2 after this treatment for these solar cells.[56] More sophisticated heat treatments are, however, required for further significant improvements. Furthermore, the physical properties of the ZnO NW/CuSCN heterojunctions are still open in addition to their relationship with the performances of the corresponding self-powered UV photodetectors, while their understanding is critical for strong improvements. In this paper, the effects of heat treatment under air and nitrogen atmospheres are thoroughly investigated on the physical properties of ZnO NW/CuSCN heterojunctions: both (1) the structural and chemical properties of the CuSCN layers deposited by impregnation technique and (2) the electrical properties of these heterojunctions are reported. The performances of self-powered UV photodetectors based on ZnO NW/CuSCN heterojunctions are eventually shown.

2. EXPERIMENTAL SECTION

2.1. Deposition Techniques. Fluorine-doped tin oxide (FTO) thin films as transparent electrodes were deposited on Corning C1737 borosilicate glass substrates by a homemade spray pyrolysis reactor.[47] The 300 nm thick standard FTO layers have a typical optical transmittance larger than 85% in the visible range and a typical electrical sheet resistance smaller than 10 Ω/sq. The layers were cleaned in acetone and then in isopropanol solution under ultrasonic waves for 10 min each. On top of FTO layers, a thin seed layer of ZnO was deposited by dip coating. The seed layer favors the control of the growth and of the structural morphology of ZnO NW arrays. A solution of zinc acetate dihydrate (ZnAc$_2$·2H$_2$O) from Merck and monoethanolamine from JT Baker dissolved in absolute ethanol was used in an equimolar ratio of 0.375M. Two postheat treatments were performed at 300 and 540 °C to remove organic compounds and to crystallize the seed layer, respectively. Subsequently, ZnO NWs were grown by chemical bath deposition. The growth was performed at 90 °C for 3 h in a solution of zinc nitrate (Zn(NO$_3$)$_2$·6H$_2$O) and hexamethylenetetramine HMTA (C$_6$H$_{12}$N$_4$) from Sigma-Aldrich dissolved in deionized water in an equimolar ratio of 0.03M. To remove all organic compounds, we performed a postheat treatment on a hot plate kept at 450 °C. To fill the pores between ZnO NWs, we deposited the CuSCN layer by impregnation technique. CuSCN (99% Sigma-Aldrich) powder was initially dissolved in n-propylsulfide (97% Sigma-Aldrich) above the solubility limit of 0.04 M, which is typically reached by mixing 0.05 g of CuSCN in 10 mL of n-propylsulfide.[23] After 24 h of stirring and 12 h of settling, a yellowish color solution was prepared. The impregnation technique subsequently consisted in depositing the solution droplet by droplet on the sample kept at 100 °C to favor solvent evaporation. The thickness was adjusted by varying the number of droplets. Annealing was then performed under air or nitrogen atmospheres in a quartz tube furnace with a flow gas rate of 2L/min. A temperature ramp of 15 °C/min was fixed with the annealing time of 1 h. The annealing temperature was varied in the range of 125 to 300 °C with a step of 25 °C. A 0.06 cm^2 surface area and 40 nm thick gold (4 N) back contact was eventually deposited on the CuSCN layer by vacuum evaporation with an Edwards evaporator. The gold thin layer favors an ohmic contact between the CuSCN layer and the metallic electrode.
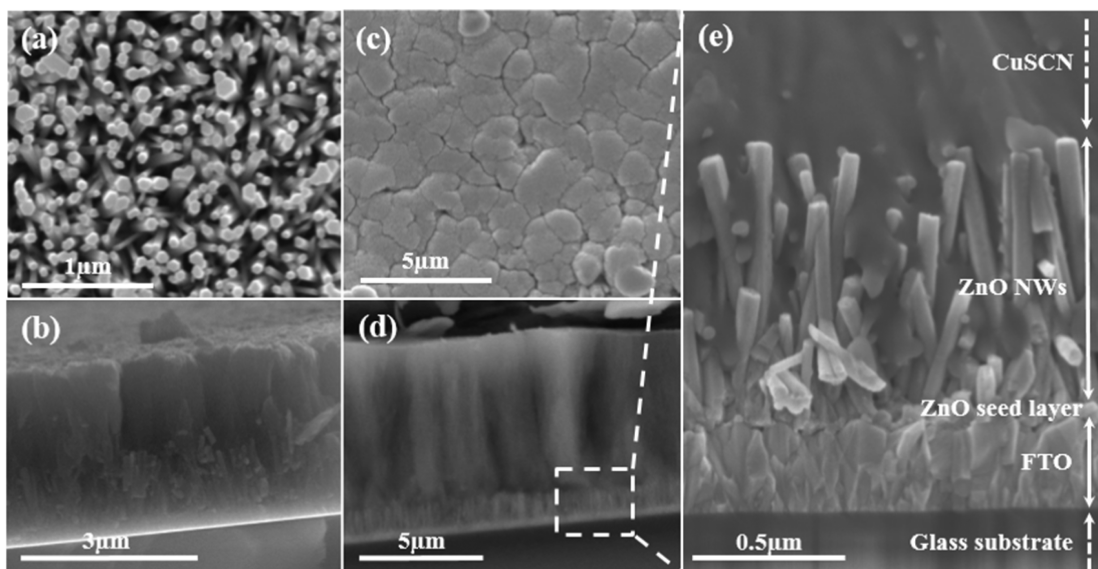
Figure 1. (a) Top-view SEM image of vertically aligned ZnO NW arrays, (b) cross-sectional SEM image of as-grown ZnO NW/1.6 μm thick CuSCN heterojunctions, (c) top-view and (d) cross-sectional SEM images of as-grown ZnO NW/7 μm thick CuSCN heterojunctions, with (e) a high-magnification image showing the impregnation of the CuSCN layer into the ZnO NW arrays.

2.2. Characterization Techniques. Field-emission scanning electron microscopy (SEM) images were recorded with a ZEISS Ultra+ microscope. X-ray diffraction (XRD) measurements were performed with a Bruker D8 Advance diffractometer using Cu Kα_1 radiation according to the Bragg–Brentano configuration. The θ–2θ XRD patterns were collected between 10 and 70° in 2θ scale. The texture analysis of the CuSCN layer was quantitatively carried out from the Kα_1 component of each diffraction peak in the framework of the Harris method:[48] the texture coefficients c_{hkl} for each $[hkl]$ crystallographic direction and the degree of preferred orientation σ were, respectively, defined as follows:

$$c_{hkl} = \frac{\frac{I_{hkl}}{I_{0,hkl}}}{\frac{1}{N}\sum^{N}\frac{I_{hkl}}{I_{0,hkl}}} \quad \text{and} \quad \sigma = \frac{\sqrt{\sum^{N}(c_{hkl}-1)^2}}{\sqrt{N}}$$

in which N is the peak number, I_{hkl} and $I_{0,hkl}$ are the intensity of the (hkl) Bragg reflection for the studied sample and for a randomly oriented sample, respectively. In our case, the following four diffraction peaks were taken into account from the 00-029-0581 file of International Center for Diffraction Data (ICDD): (003), (101), (110), and (113). The diffraction peaks from CuSCN with a very low intensity or located close to the diffraction peaks of ZnO were not considered. In the case of $N = 4$, the texture coefficient $c_{hkl} = 1$ and the degree of preferred orientation $\sigma = 0$ are correlated with a randomly oriented sample whereas $c_{hkl} = 4$ and $\sigma = (N-1)^{1/2} = 1.73$ indicate a perfectly oriented sample.

Raman scattering measurements were collected using a Jobin Yvon/Horiba Labram spectrometer equipped with a liquid nitrogen cooled coupled charge device detector. The experiments were conducted in the micro-Raman mode at room temperature in a backscattering geometry. The Raman spectra were recorded from the film surface. The 488 nm line of an Ar$^+$ laser was focused to a spot size smaller than 1 μm on the sample with a power limited to 90 μW in order to prevent the degradation of the CuSCN layer. Raman spectra were calibrated using Si at room temperature. Energy dispersive X-ray (EDX) analysis was achieved with a Bruker detector incorporated on a field-emission SEM Quanta 250 to estimate the stoichiometry of the CuSCN layer, which is defined as the ratio of [Cu]/[SCN]. This ratio controls the type of semiconductor: n-type CuSCN is reached for [Cu]/[SCN] > 1 (i.e., copper-rich sample) while p-type CuSCN is reached for [Cu]/[SCN] < 1 (i.e., copper-poor sample). However, carbon and nitrogen are too light to allow accurate EDX measurements such that the

stoichiometry is only assessed by the ratio of copper over sulfur elements.[49] Current-density versus voltage (J–V) characteristics of the heterojunctions were determined in dark conditions using a Keithley 2400 and controlled using Labview 8.6 software. Absorption measurements were performed with a UV–visible–NIR PerkinElmer Lambda 950 spectrophotometer equipped with an integrating sphere for determining the total transmittance and reflectance. The photovoltaic performances were recorded under 100 mW/cm^2 AM 1.5G simulated sunlight with a calibrated solar simulator from Oriel Instruments. The responsivity of the ZnO NW/CuSCN heterojunctions was measured at room temperature using a xenon lamp, monochromator, chopper, and lock-in amplifier.

3. RESULTS AND DISCUSSION

3.1. Structural Properties of ZnO NW/As-Grown CuSCN Heterojunctions. The typical structural morphologies of ZnO NW arrays and related ZnO NW/as-grown CuSCN heterojunctions are shown by top-view and cross-sectional SEM images in Figure 1. The deposition of the seed layer was optimized on top of FTO/glass substrates by taking into account the FTO thin film roughness and texture in order to form relatively dense ZnO NW arrays.[47] ZnO NWs are fairly well vertically aligned with a mean diameter, length, and density of about 90 nm, 1 μm, and 70 NW/μm^2, respectively. ZnO NWs with a relatively short length are formed in order to favor the subsequent high impregnation of the CuSCN layer (i.e., a good pore-filling), as shown in the SEM image of Figure 1e. ZnO NWs have a wurtzite crystalline structure and are oriented along the polar c axis,[12] as revealed by the most intense ZnO diffraction peak indexed with green circle in the XRD patterns of Figure 2. The other minor ZnO diffraction peaks indexed with green circles originate from the polycrystalline seed layer composed of ZnO NPs with a large number of different orientations although this layer is textured along the polar c axis.

The 1.6 and 7 μm thick CuSCN layers were deposited by using 5 and 15 droplets, respectively, as shown by cross-sectional SEM images in Figure 1b,d. The CuSCN layer exhibits a columnar grain structure with a typical size in the range of 80–110 nm, resulting in a slightly rough free surface
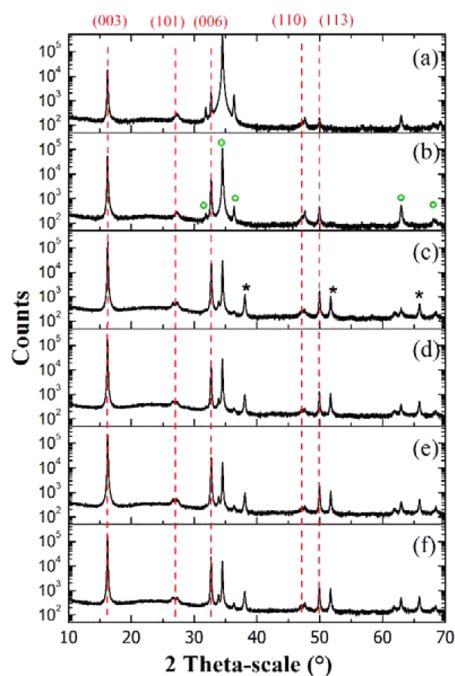
Figure 2. XRD patterns of as-grown ZnO NW/CuSCN heteronjunctions with the CuSCN layer thickness of (a) 1.6 and (b) 7 μm. XRD patterns of ZnO NW/7 μm thick CuSCN heterojunctions annealed at (c) 150 and (d) 200 °C under air atmosphere. XRD patterns of ZnO NW/7 μm thick CuSCN heterojunctions annealed at (e) 150 and (f) 200 °C under nitrogen atmosphere. (Green ○) ZnO diffractions peaks (wurtzite phase, 00-036-1451 file from ICDD); (★) FTO diffractions peaks (cassiterite phase, 00-041-1445 file from ICDD); and (red dashed lines) β-CuSCN diffraction peaks (rhombohedral phase, 00-029-0581 file from ICDD).

that is typical of polycrystalline semiconductor thin films with a columnar grain structure. The occurrence of cracks between grains are clearly shown for the 7 μm thick CuSCN layer in Figure 1c and more likely arises from mud-cracking effects. The mud-cracking is due to the slow evaporation of n-propylsulfide from the CuSCN layer and can form cavities and voids.[54] The XRD patterns of 1.6 and 7 μm thick CuSCN layers are shown in Figure 2. Basically, the CuSCN compound can grow with the two polymorphic crystalline structures, which are the orthorhombic α-phase,[50] and the rhombohedral β-phase (trigonal pyramidal structure).[51,52] It is expected that the rhombohedral β-phase is more commonly formed and more stable. This statement holds in the present case, for which the crystalline structure of 1.6 and 7 μm thick CuSCN layers corresponds to the rhombohedral β-phase, as shown by the red dashed lines in Figure 2. Interestingly, both the CuSCN layers exhibit the same [003] strong preferential orientation. The [003] texture coefficient c_{003} is typically about 3.7 for a maximum of 4. In contrast, the other calculated [101], [110], and [113] texture coefficients c_{101}, c_{110}, and c_{113} are smaller than 1. The degree of preferred orientation of 1.6 is also very high, leading to a relative degree of preferred orientation larger than 90%. It has been shown that the texture of the CuSCN layer is strongly dependent upon the deposition technique.[50,51] The preferential orientation usually occurs along the [101] and [003] directions for low and high concentrations of chemical precursors in electrodeposition, respectively.[53] In contrast, the preferential orientation along the [003] direction has already been reported when deposited by impregnation techniques.[51]

The strong preferential orientation is fairly unusual for polycrystalline semiconductor thin films, in which the anisotropy of the crystalline phases is generally not highly pronounced. This may originate from the columnar grain structure in the CuSCN layer, as shown in Figure 1, combined with the crystalline structure of the CuSCN compound. According to the rhombohedral β-phase, the layers of SCN ions separate the planes of Cu atoms and strong Cu−S bonds three-dimensionally interconnect these layers. This crystalline structure with a polymeric form[51,52] might account for the formation of the strong preferential orientation along the [003] direction, which is normal to the parallel alignment of the SCN groups. Also, it should be noted that the XRD pattern signals mainly come from the CuSCN bulk on top of ZnO NWs such that the preferential orientation could also be due to standard thickening process at very low deposition temperature. As a consequence, it is expected that the preferential orientation of the CuSCN layer between ZnO NWs is less pronounced.

3.2. Structural and Chemical Properties of Annealed ZnO NW/CuSCN Heterojunctions. To assess the potential of the simplest postgrowth treatment, we achieved an in situ solvent outgassing from ZnO NW/as-grown CuSCN heterojunctions at the growth temperature of 100 °C for 1, 3, and 21.5 h. Interestingly, the significant band assigned to the ν(C−H) of n-propylsulfide[59] in the 2900−3000 cm^{-1} range of the Raman spectra is strongly decreased after 3 h of outgassing (Supporting Information, Figure S1). The relative high boiling point of T_b = 142 °C for the n-propylsulfide solvent as compared to the outgassing temperature of 100 °C may account for the long duration needed for removing the solvent from the CuSCN layer. Additionally, the long outgassing is found to improve the electrical properties of the ZnO NW/CuSCN heterojunctions. RR as deduced by the ratio of the current at the forward voltage (+2 V) over the current at the reverse voltage (−2 V) on J−V measurements (Supporting Information, Figure S2) is relatively low (i.e., <100) for as-grown ZnO NW/CuSCN heterojunctions and after 1 h of outgassing, respectively. An improvement of 1 order of magnitude has been reached after 21.5 h-long outgassing, in which RR (±2 V) is equal to 420, but longer outgassing effects are still limited (i.e., RR (±2 V) = 652 after 30 h of outgassing).

To go further than a simple solvent outgassing, we considered different thermal heat treatments in the following on ZnO NW/CuSCN heterojunctions by changing both annealing temperature and atmosphere conditions. No thermal heat effects on the structural morphology of ZnO NW/CuSCN heterojunctions are revealed by SEM images. The XRD patterns of ZnO NW/CuSCN heterojunctions annealed under air and nitrogen atmospheres at 150 and 200 °C are shown in Figure 2. These XRD patterns are very similar to the XRD patterns of as-grown ZnO NW/CuSCN heterojunctions. The main texture coefficient c_{003} still has the same value of 3.7, while the degree of preferred orientation is still very high and about 1.6, regardless of the annealing temperature and atmosphere. Neither change in the structural morphology nor the occurrence of another crystalline phase (i.e., oxide or binary phase) are even revealed for a relatively high annealing temperature of 200 °C under air atmosphere. In the present range of annealing temperature, no change of the crystalline phase of CuSCN thus occurs under air or nitrogen atmospheres, and the preferential orientation along the [003] direction is still strongly pronounced.

The Raman spectra of ZnO NW/CuSCN heterojunctions annealed under air and nitrogen atmospheres are shown in Figure 3. Most of the Raman lines are attributed to the CuSCN
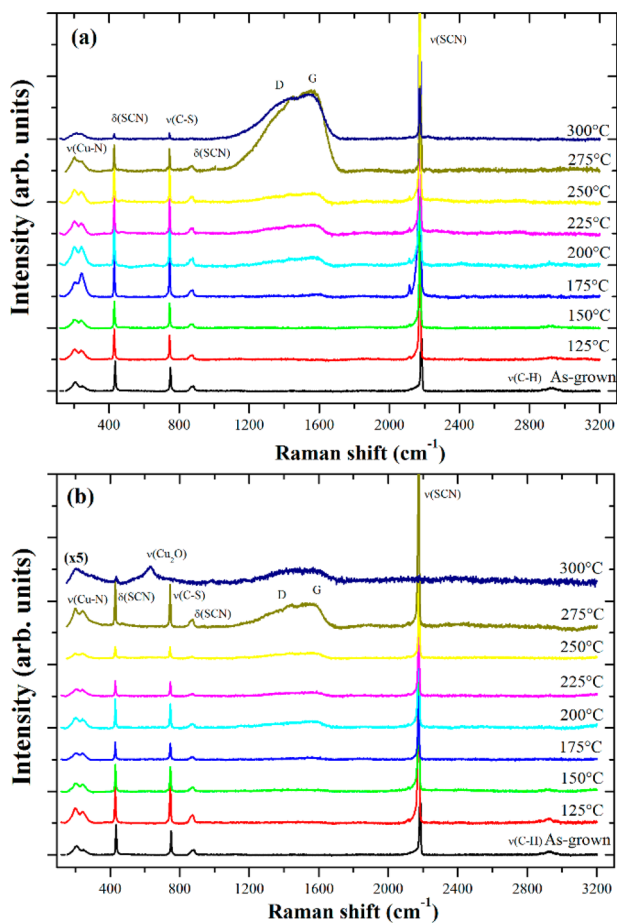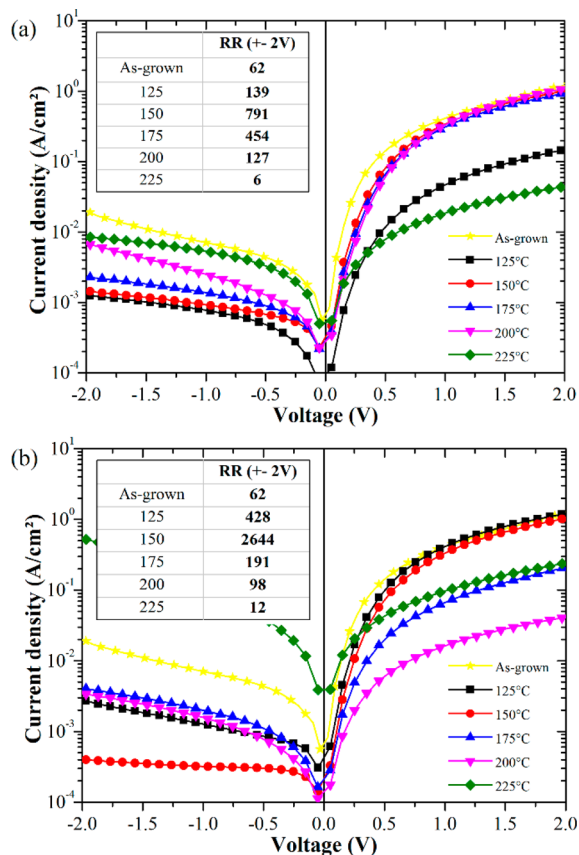

Figure 3. Room-temperature Raman scattering measurements of ZnO NW/7 μm thick CuSCN heterojunctions annealed under (a) nitrogen and (b) air atmospheres in the temperature range of 100−300 °C.

crystalline phase, and especially to the rhombohedral β-phase.[57,58] The intense line at 2174 cm^{-1} is attributed to the bridging thiocyanate group region ν(SCN), precisely the stretching ν(C−N) mode. The 429.5 and 745 cm^{-1} lines are assigned to the δ(SCN) bending and ν(C−S) stretching modes, respectively. The broad band at 874 cm^{-1} is an overtone of the δ(SCN) mode. The two contributions around 200 and 242 cm^{-1} could tentatively be assigned to Cu−N and Cu−S vibration modes, respectively, according to ref 55. Importantly, no binary phases are detected as the annealing temperature is raised to 275 °C under air atmosphere, which is in agreement with XRD patterns. However, a copper oxide (Cu$_2$O) crystalline phase is formed at the highest annealing temperature of 300 °C under air atmosphere, as shown by the occurrence of lines at 220 and 636 cm^{-1} (Figure 3b) that are related to the two major lines of Cu$_2$O.[60,61] Nevertheless, no Raman lines related to copper sulfide occur in the spectrum at 472 and 474 cm^{-1}, for ν(Cu$_2$S) and ν(CuS), respectively.[62] At lower annealing temperature, the residual solvent signature is still observed in the CuSCN layer. Indeed, the annealing is only 1 h long, and hence, outgassing processes are not completed, as shown previously. Thus, the intensity of the weak band at 2900 cm^{-1} assigned to the ν(C−H) of n-propylsulfide[59] decreases as

the annealing temperature is raised. The residual solvent is no longer detected from the annealing temperature of 150 °C, which is just above the boiling point of the n-propylsulfide solvent of T_b = 142 °C. As a consequence, 1 h of annealing above the boiling point of solvent is enough to remove the excess of solvent from the CuSCN layer. Furthermore, a weak intensity peak lying in the region of the stretching thiocyanate group at 2120 cm^{-1} is attributed to (CuSCN)$_x$ aggregates.[57] It becomes more intense after annealing at 175 °C and then decreases at higher annealing temperature. The formation of these aggregates accounts for the decomposition process of the CuSCN layer. Besides, a new band appears around 1600 cm^{-1} from the annealing temperature of 175 °C, and its intensity still increases by further raising the annealing temperature. From the annealing temperature of 275 °C under nitrogen and air atmospheres, this band gives rise to two very broad lines centered at 1590 and 1404 cm^{-1}. These lines typically reveal the formation of amorphous carbon. The first line around 1580−1600 cm^{-1} is called the G peak for "graphitic-like structure", and the second line around 1350 cm^{-1} is called the D peak for "diamond-like structure".[63] Additionally, a brown coloration of the samples is systematically observed for annealing temperatures higher than 175 °C, indicating again that the decomposition process of the CuSCN layer proceeds at relatively low annealing temperature. Two distinct physical phenomena might be related: the first process could be related to the degradation of the polycrystalline structure of CuSCN forming (CuSCN)$_x$ aggregates while the second process could involve the decomposition of these aggregates into amorphous carbon. Interestingly, copper oxide is detected under air atmosphere as the annealing temperature of 300 °C is reached, as shown by the Raman lines at 220 and 636 cm^{-1}.[60,61] The oxidation of the CuSCN layer thus begins around the annealing temperature of 300 °C. Interestingly, the [Cu]/[S] ratio as determined by EDX measurements starts increasing from the annealing temperatures of 250 and 300 °C under air and nitrogen atmosphere, respectively, and is marked by a reduction of the sulfur content (Supporting Information, Table S1). Additionally, nanoparticles of presumably pure copper are formed on top of the CuSCN layer from the annealing temperature of 250 °C under nitrogen atmosphere (Supporting Information, Figure S3).

3.3. Electrical Properties of Annealed ZnO NW/CuSCN Heterojunctions. J−V measurements of ZnO NW/CuSCN heterojunctions annealed under air and nitrogen atmospheres are shown in Figure 4. A table of RRs is reported in the inset of Figure 4. All the diodes exhibit a clear rectifier behavior. Owing to the high level of the diode series resistance, the current density (J) in Figure 4 starts saturating for voltages (V) larger than 1 V. For instance, ZnO NW/CuSCN heterojunctions annealed at the temperature of 150 °C under air atmosphere has a high series resistance of about 23 $\Omega\cdot$cm^2, which is more likely due to the low conductivity of the CuSCN layer. Additionally, the diode ideality factor in the low voltage range of 0.05−0.4 V is found to be about 4. This large ideality factor may be due to (1) the poor filling of ZnO NW arrays by the CuSCN layer or (2) the occurrence of surface/interface states.[64] Nonetheless, the filling of ZnO NW arrays by the CuSCN layer is clearly completed as shown in Figure 1. In contrast, it has been demonstrated that the electrical properties of ZnO NW/CuSCN heterojunctions are drastically affected by the annealing of ZnO NWs under variable conditions.[34] Consequently, the interface quality of ZnO NW/CuSCN

Figure 4. *J*−*V* measurements of ZnO NW/7 μm thick CuSCN heterojunctions annealed under (a) nitrogen and (b) and air atmospheres. The values of the rectification ratio RR at ±2 V are reported in the tables in inset.

Table 1. Rectification Ratio (RR) of the Diodes Composed of ZnO NW/CuSCN Heterojunctions

ref	deposition technique	RR
Ni et al.[30]	electrodeposition	19 (±0.5 V)
Wu et al.[31]	electrodeposition	154 (±2 V)
Zhang et al.[32]	electrodeposition	3 (±4 V)
Gertman et al.[35]	pulsed electrodeposition	1070 (±2 V)
Hatch et al.[33]	spray	3550 (±3 V)
	impregnation	1240 (±3 V)
Hatch et al.[34]	spray, as-grown NW	3 (±3 V)
	spray, O$_2$ annealed NW	440 (±3 V)
	spray, N$_2$ annealed NW	600 (±3 V)
	spray, air annealed NW	21500 (±3 V)
our work (150 °C, air)	impregnation	2644 (±2 V)
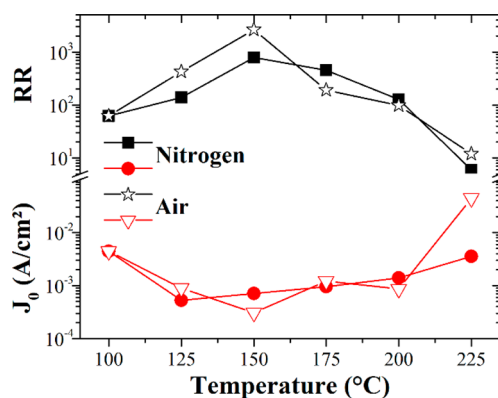
Figure 5. Evolution of RR and *J*$_0$ for ZnO NW/7 μm thick CuSCN heterojunctions as a function of annealing temperature under (black ☆ and red ▽) air and (black ■ and red ●) nitrogen atmospheres.

heterojunctions is expected to play a crucial role on the electrical properties. The dependence of *J*−*V* measurements on the annealing temperature is identical under both air and nitrogen atmospheres. The electrical performances are initially improved as the annealing temperature is raised to 150 °C and subsequently deteriorated for higher annealing temperature. The best improvement is achieved at the annealing temperature of 150 °C, for which the RRs of 791 and 2644 at ±2 V are determined under nitrogen and air atmospheres, respectively. The annealing under oxidizing air atmosphere is therefore more beneficial than the annealing under neutral nitrogen atmosphere. Importantly, the best RR value of 2644 at ±2 V, we have determined, is the highest value reported for ZnO NW/CuSCN heterojunctions deposited by impregnation techniques, as presented in Table 1. It is worth noticing that the highest value of RR up to 21500 at ±3 V has been reached by changing the surface states of ZnO NWs following an annealing under air atmosphere prior to the CuSCN deposition.[34] This indicates that one of the major effects at the annealing temperature of 150 °C is the improvement of the interface properties between the ZnO NWs and CuSCN layer.

The evolutions of RR and *J*$_0$ are reported as a function of annealing temperature in Figure 5 for both annealing under air and nitrogen atmospheres. Interestingly, as regards the annealing under air (respectively nitrogen) atmosphere, the initial increase in the RR from 62 to 2644 (respectively 791) is related to the decrease in the average reverse current density *J*$_0$ (i.e., as calculated by averaging the reverse current in the

voltage range of −0.4 to −0.05 V) from 4.5 × 10^{-3} A/cm^2 for as-grown ZnO NW/CuSCN heterojunctions to 3.1 × 10^{-4} A/cm^2 (respectively 7.1 × 10^{-4} A/cm^2) for ZnO NW/CuSCN heterojunctions annealed at 150 °C. *J*$_0$ subsequently increases for higher annealing temperature to 4.5 × 10^{-2} A/cm^2 (respectively 3.6 × 10^{-3} A/cm^2) and hence RR decreases down to 12 (respectively 6). The reduction of *J*$_0$ at the annealing temperature of 150 °C is thus correlated strongly with the optimal value of RR for both annealing under air and nitrogen atmospheres. At this temperature, the solvent is fully removed, as previously shown by Raman scattering measurements in Figure 3. A smaller density of recombination centers correlated with a decrease in the density of defects might occur after annealing and hence give rise to a smaller *J*$_0$. Another annealing effect is due to the variation of the diode shunt resistance for annealing temperature higher than 125 °C. The shunt resistance was estimated by calculating the slope of the *J*−*V* curve close to zero bias voltage. A shunt resistance of a few hundreds of Ω·cm^2 is deduced for the annealing temperatures of 125 and 150 °C. In contrast, a decrease in the shunt resistance occurs down to a few tens of Ω·cm^2 for annealing temperature higher than 200 °C. Thus, the deterioration of the electrical performances at higher annealing temperature can be correlated with the formation of amorphous carbon and/or of copper nanoparticles, as shown previously by Raman scattering and EDX measurements: this may create shunted paths and, as a consequence, decrease the shunt resistance at higher annealing temperatures.

3.4. Performances of Self-Powered UV Photodetectors.

A schematic of the self-powered UV photodetector together with the corresponding energy band diagram are reported in Figure 6. The UV illumination is made from the
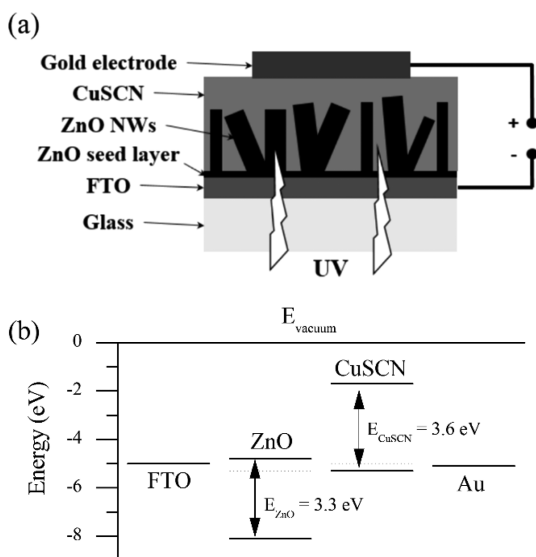

Figure 6. Schematics of (a) the self-powered UV photodetector based on ZnO NW/CuSCN heterojunctions and (b) of the corresponding energy band diagram. The UV illumination is made from the FTO/glass substrate side.

FTO/glass substrate side such that the electron−hole pairs are mainly photogenerated in the ZnO NWs through the absorption of UV incident photons. To a lesser extent, the CuSCN layer may also contribute to the photogeneration of electron−hole pairs; nevertheless, this is much less likely because the light first propagates through the FTO thin films with a quite similar band gap energy. The electron−hole pairs photogenerated in the ZnO NWs are then separated by the built-in voltage in the heterojunctions. The electrons and holes are, respectively, collected by the FTO thin film via the ZnO NWs and by the gold contact via the CuSCN layer. The UV photodetector is based on a p-n heterojunction, and hence, the responsivity can arise from three distinct contributions: (1) the n-layer of ZnO NWs, (2) the space charge region and (3) the p-layer of CuSCN. In our case, the built-in voltage is smaller than 0.5 V due to the difference in work function W between CuSCN ($W \approx 5$ eV)[23] and ZnO ($W \approx 5.3$ eV).[65] The contribution from the space charge region may therefore be neglected to a first approximation. As a consequence, a major contribution from the n-layer of ZnO NWs and possibly a minor contribution from the p-layer of CuSCN are expected to predominantly drive the responsivity.

The effects of the structural morphology of ZnO NW/CuSCN heterojunctions are investigated on the performances of the UV photodetectors by varying the length of ZnO NWs. ZnO NW/CuSCN heterojunctions involving ZnO NWs with three different lengths (1, 1.5, and 2 μm) were fabricated for a given 7 μm thick CuSCN layer. These ZnO NW/7 μm thick CuSCN heterojunctions were annealed at 150 °C under air atmosphere to improve their electrical performances, as discussed previously, and eventually integrated as UV photodetectors. The absorption of the ZnO NW/CuSCN heterojunctions and the related responsivity of the full UV

photodetectors are shown in Figure 7a. The sharp cut of absorption around 400 nm is related to the main peak of
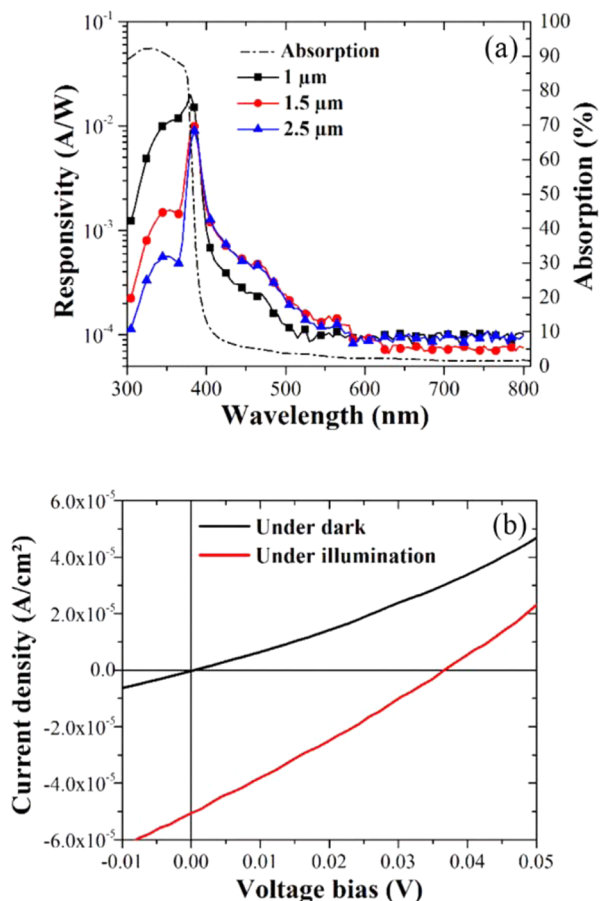
Figure 7. (a) Absorption measurements of ZnO NW/7 μm thick CuSCN heterojunctions annealed at 150 °C under air atmosphere and responsivity measurements of the corresponding self-powered UV photodetectors with 1, 1.5, and 2.5 μm long ZnO NWs. (b) J−V measurements of the self-powered UV photodetectors consisting of ZnO NW/7 μm thick CuSCN heterojunctions annealed at 150 °C under air atmosphere collected under darkness and illumination conditions.

responsivity at 370 nm, which is close to the ZnO band gap wavelength of 375 nm (i.e., 3.3 eV) and hence ascribed to the n-layer contribution. The UV photodetection is therefore favored in the wavelength range smaller than 380 nm. It is expected that the main peak is due to the efficient extraction and collection of electron−hole pairs that are photogenerated in the ZnO NWs covered with the CuSCN layer. The maximum responsivity at 370 nm is $R_{370 \text{ nm}} = 0.02$ A/W for 1 μm long ZnO NWs and decreases down to 0.01 A/W for 1.5 and 2 μm long ZnO NWs. Also, the related UV-to-visible (370−500 nm) rejection ratio of the UV photodetector is about 100. It should be noted that the maximum responsivity of 0.02 A/W at zero bias is higher than that in ref 37 for an identical rejection ratio, but the excitation conditions were distinct, that is, $R_{375 \text{ nm}} = 0.0075$ A/W for 6 mW cm^{-2} irradiance and a minimum UV-to-visible rejection ratio of ∼100. A second significant peak is centered (i.e., 3.55 eV), for which the maximum responsivity at 350 nm is $R_{350 \text{ nm}} = 0.01$ A/W. Importantly, the intensity of the second peak is strongly reduced by increasing the ZnO NW length for a given 7 μm

thick CuSCN layer. Basically, the impregnation of the CuSCN layer is improved for shorter ZnO NWs, as shown in Figure 1e, such that the extraction and collection of photogenerated electron−hole pairs in ZnO NWs is increased. Because the absorption depth is decreased by reducing the wavelength, the electron−hole pairs are predominantly photogenerated at the bottom of the ZnO NWs in the present case. Accordingly, the extraction and collection of the photogenerated holes are less efficient because they must cross the entire CuSCN layer, leading to a decrease in the responsivity as the wavelength gets shorter. Moreover, the FTO thin films can also absorb the light at these short wavelengths before coming into the ZnO NW/CuSCN heterojunctions. Eventually, the second peak, although more pronounced, is less intense for longer ZnO NWs because the impregnation of the CuSCN layer is expected to be less controlled: the electron hole pairs are thus mainly photogenerated in ZnO NWs with no CuSCN layer forming the heterojunctions, which is detrimental for their separation. As a consequence, the wavelength selectivity of 370 nm for the UV photodetector is reinforced by the increase in the ZnO NW length. By changing the structural morphology of ZnO NW/CuSCN heterojunctions, the selectivity of the UV photodetector can thus be readily modulated.

Furthermore, $J−V$ measurements of ZnO NW/CuSCN heterojunctions under dark and illumination conditions are shown in Figure 7b. The open-circuit voltage (V_{OC}), short-circuit current density (J_{SC}), and fill factor (FF) are 37 mV, 51 $\mu A/cm^2$, and 27.1%, respectively. The relatively high V_{OC} of 37 mV is determined here as compared to ref 37, in which a low V_{OC} of about 1 mV was reported. Owing to the beneficial annealing process at 150 °C, it turns out that the decrease in the reverse current density J_0 favors a fairly good V_{OC} by decreasing the density of interfacial defects. Such a significant photovoltaic effect with wide band gap semiconductor heterojunctions may be useful for the self-powering of the UV photodetector when connected with an external battery, for instance. Eventually, ZnO NW/CuSCN heterojunctions are fairly stable in time and still exhibit a significant photovoltaic effect, even after 1 year when stored under atmospheric conditions (Supporting Information, Figure S4). Such good stability is one asset of CuSCN[23,26,56] and is promising for their real-world integration as self-powered UV photodetectors.

4. CONCLUSION

The annealing effects under air and nitrogen atmospheres are investigated in a wide range of temperature on the physical properties of ZnO NW/CuSCN heterojunctions and the performances of the corresponding self-powered UV photodetectors. The as-grown CuSCN layer as deposited by impregnation technique is found polycrystalline with the β-rhombohedral crystalline phase. The columnar grains have a typical size in the range of 80−110 nm and are strongly oriented along the [003] direction owing to the polymeric form of the β-rhombohedral crystalline phase. Importantly, the CuSCN layer completely fills in ZnO NW arrays from their bottom to their top, demonstrating the homogeneous formation of ZnO NW/CuSCN heterojunctions. No modifications in the structural properties of the CuSCN layer are revealed by SEM images and XRD patterns after outgassing or annealing, regardless of time, temperature, or atmosphere. The Raman scattering measurements indicate that the solvent can beneficially be outgased from the CuSCN from the growth temperature of 100 °C after several tens of hours or from the

annealing temperature of 150 °C after only 1 h. In contrast, a strong degradation of the CuSCN layer turns out from the higher annealing temperature of 175 °C, for which both amorphous carbon and binary phases are formed while the sulfur content is reduced. Concerning the $J−V$ measurements of the ZnO NW/CuSCN heterojunctions, it is demonstrated that the outgassing is a necessary step to improve the electrical performances. Three hours of outgassing is typically enough to remove all solvent from the CuSCN layer. However, the $J−V$ measurements are still limited by this single step of outgassing: RR (± 2 V) = 652 after 30 h. It is further shown that the annealing under both atmospheres can first improve the RR up to the annealing temperature of 150 °C, which then decreases at higher annealing temperature. This is correlated with the CuSCN layer properties: (1) the outgassing of solvent at low annealing temperature improves the $J−V$ performance, (2) the annealing around 150 °C may decrease the density of defects at the interfaces, such that the reverse current J_0 is decreased, leading to the best value of RR (± 2 V) = 2644, and (3) the degradation of the CuSCN layer creates shunt paths and so reduces the $J−V$ performance. Finally, we demonstrate the efficient integration of ZnO NW/CuSCN heterojunctions as self-powered UV photodetectors with a maximum responsivity of 0.02 A/W at zero bias and at 370 nm under an irradiance of 100 mW/cm². The selectivity of the self-powered UV photodetector can further by modulated by varying the length of ZnO NWs. Eventually, a significant photovoltaic effect of the device is measured with V_{OC} = 37 mV and J_{SC} = 51 $\mu A/cm^2$, which could ensure the self-powering of the complete device.

■ ASSOCIATED CONTENT

ⓢ Supporting Information
Variation of the [Cu]/[S] ratio determined by EDX measurements; Raman scattering measurements of outgassed ZnO NW/7 μm thick CuSCN heterojunctions; $J−V$ measurements of heterojunctions annealed at 100 °C under air atmospheres;top-view SEM and BSE images of heterojunctions annealed at 275 °C under nitrogen atmosphere; and $J−V$ measurements of ZnO NW/7 μm thick CuSCN heterojunctions under illumination as-deposited and after one year old stored under atmospheric conditions. This material is available free of charge via the Internet at http://pubs.acs.org.

■ AUTHOR INFORMATION

Corresponding Author
*E-mail: garnier.jerome.1@gmail.com.
Notes
The authors declare no competing financial interest.

■ REFERENCES

(1) Ozgur, U.; Alivov, Y. I.; Liu, C.; Teke, A.; Reshchikov, M. A.; Dogan, S.; Avrutin, V.; Cho, S. J.; Morkoc, H. A Comprehensive Review of ZnO Materials and Devices. *J. Appl. Phys.* **2005**, *98*, 1−103.
(2) Xu, S.; Wang, Z. L. One-Dimensional ZnO Nanostructures: Solution Growth and Functional Properties. *Nano Res.* **2011**, *11*, 1013−1098.

(3) Kong, Y. C.; Yu, D. P.; Zhang, B.; Fang, W.; Feng, S. Q. Ultraviolet-Emitting ZnO Nanowires Synthesized by a Physical Vapor Deposition Approach. *Appl. Phys. Lett.* **2001**, *78*, 407−409.

(4) Yao, B. D.; Chan, Y. F.; Wang, N. Formation of ZnO Nanostructures by a Simple Way of Thermal Evaporation. *Appl. Phys. Lett.* **2002**, *81*, 757−759.

(5) Sun, Y.; Fuge, G. M.; Ashfold, M. N. R. Growth of Aligned ZnO Nanorod Arrays by Catalyst-Free Pulsed Laser Deposition Methods. *Chem. Phys. Lett.* **2004**, *396*, 21−26.

(6) Zheng, M. J.; Zhang, L. D.; Li, G. H.; Shen, W. Z. Fabrication and Optical Properties of Large-Scale Uniform Zinc Oxide Nanowire Arrays by One-Step Electrochemical Deposition Technique. *Chem. Phys. Lett.* **2002**, *363*, 123−128.

(7) Vayssieres, L.; Keis, K.; Lindquist, S. E.; Hagfeldt, A. J. Purpose-Built Anisotropic Metal Oxide Material: 3D Highly Oriented Microrod Array of ZnO. *J. Phys. Chem. B* **2001**, *105*, 3350−3352.

(8) Yamabi, S.; Imai, H. J. Growth Conditions for Wurtzite Zinc Oxide Films in Aqueous Solutions. *J. Mater. Chem.* **2002**, *12*, 3773−3778.

(9) Govender, K.; Boyle, D. S.; O'Brien, P.; Binks, D.; West, D.; Coleman, D. Room-Temperature Lasing Observed from ZnO Nanocolumns Grown by Aqueous Solution Deposition. *Adv. Mater.* **2002**, *14*, 1221−1224.

(10) Greene, L. E.; Law, M.; Goldberger, J.; Kim, F.; Johnson, J. C.; Zhang, Y.; Saykally, R. J.; Yang, P. Low-Temperature Wafer-Scale Production of ZnO Nanowire Arrays. *Angew. Chem., Int. Ed.* **2003**, *42*, 3031−3034.

(11) Choy, J. H.; Jang, E. S.; Won, J. H.; Chung, J. H.; Jang, D. J.; Kim, Y. W. Soft Solution Route to Directionally Grown ZnO Nanorod Arrays on Si Wafer; Room-Temperature Ultraviolet Laser. *Adv. Mater.* **2003**, *15*, 1911−1914.

(12) Guillemin, S.; Consonni, V.; Appert, E.; Puyoo, E.; Rapenne, L.; Roussel, H. Critical Nucleation Effects on the Structural Relationship Between ZnO Seed Layer and Nanowires. *J. Phys. Chem. C* **2012**, *116*, 25106−25111.

(13) Guillemin, S.; Rapenne, L.; Roussel, H.; Sarigiannidou, E.; Brémond, G.; Consonni, V. Formation Mechanisms of ZnO Nanowires: The Crucial Role of Crystal Orientation and Polarity. *J. Phys. Chem. C* **2013**, *117*, 20738−20745.

(14) Michallon, J.; Bucci, D.; Morand, A.; Zanuccoli, M.; Consonni, V.; Kaminski-Cachopo, A. Light Trapping in ZnO Nanowire Arrays Covered with an Absorbing Shell for Solar Cells. *Opt. Express* **2014**, *22*, A1174−A1189.

(15) Yi, G. C.; Wang, C.; Park, W. I. ZnO Nanorods: Synthesis, Characterization and Applications. *Semicond. Sci. Technol.* **2005**, *20*, S22−S34.

(16) Zhang, Q.; Dandeneau, C. S.; Zhou, X.; Cao, G. ZnO Nanostructures for Dye-Sensitized Solar Cells. *Adv. Mater.* **2009**, *41*, 4087−4108.

(17) Tena-Zaera, R.; Katty, A.; Bastide, S.; Lévy-Clément, C.; O'Regan, B.; Munoz-Sanjose, V. ZnO/CdTe/CuSCN, a Promising Heterostructure to Act as Inorganic Eta-Solar Cell. *Thin Solid Films* **2005**, *483*, 372−377.

(18) Puyoo, E.; Rey, G.; Appert, E.; Consonni, V.; Bellet, D. Efficient Dye-Sensitized Solar Cells Made from ZnO Nanostructure Composites. *J. Phys. Chem. C* **2012**, *116*, 18117−18123.

(19) Emin, S.; Singh, S. P.; Han, L.; Satoh, N.; Islam, A. Colloidal Quantum Dot Solar Cells. *Sol. Energy* **2011**, *85*, 1264−1282.

(20) Granqvist, C. G. Transparent Conductors as Solar Energy Materials: A Panoramic Review. *Sol. Energy Mater. Sol. C* **2007**, *91*, 1529−1598.

(21) Lee, Y. M.; Hsu, C. H.; Chen, H. W. Structural, Optical, and Electrical Properties of p-Type NiO Films and Composite TiO$_2$/NiO Electrodes for Solid-State Dye-Sensitized Solar Cells. *Appl. Surf. Sci.* **2009**, *8*, 4658−4663.

(22) Yang, L.; Zhang, Z.; Fang, S.; Gao, X.; Obata, M. Influence of the Preparation Conditions of TiO$_2$ Electrodes on the Performance of Solid-State Dye-Sensitized Solar Cells with CuI as a Hole Collector. *Sol. Energy* **2007**, *6*, 717−722.

(23) Kumara, G. R. R. A.; Konno, A.; Senadeera, G. K. R.; Jayaweera, P. V. V.; De Silva, D. B. R. A.; Tennakone, K. Dye-Sensitized Solar Cell with the Hole Collector p-CuSCN Deposited from a Solution in n-Propyl Sulphide. *Sol. Energy Mater. Sol. C* **2001**, *69*, 195−199.

(24) Jaffe, J. E.; Kaspar, T. C.; Droubay, T. C.; Varga, T.; Bowden, M. E.; Exarhos, G. J. Electronic and Defect Structures of CuSCN. *J. Phys. Chem. C* **2010**, *114*, 9111−9117.

(25) Perera, V. P. S.; Senevirathna, M. K. I.; Pitigala, P.K.D.D.P.; Tennakone, K. Doping CuSCN Films for Enhancement of Conductivity: Application in Dye-Sensitized Solid-State Solar Cells. *Sol. Energy Mater. Sol. C* **2005**, *86*, 443−450.

(26) Premalal, E. V. A.; Dematage, N.; Kumara, G. R. R. A.; Rajapakse, R. M. G.; Shimomura, M.; Murakami, K.; Konno, A. Preparation of Structurally Modified, Conductivity Enhanced-p-CuSCN and its Application in Dye-Sensitized Solid-State Solar Cells. *J. Power Sources* **2012**, *203*, 288−296.

(27) Tennakone, K.; Jayatissa, A. H.; Fernando, C. A. N.; Wickramanayake, S.; Punchihewa, S.; Weerasena, L. K.; Premasiri, W. D. R. Semiconducting and Photoelectrochemical Properties of n- and p-Type β-CuSCN. *Phys. Status Solidi A* **1987**, *103*, 491−497.

(28) Liu, C.; Wu, W.; Liu, K.; Li, M.; Hu, G.; Xu, H. Orientation Growth and Electrical Property of CuSCN Films Associated With the Surface States. *CrystEngComm* **2012**, *14*, 6750−6754.

(29) Sankapal, B. R.; Goncalves, E.; Ennaoui, A.; Lux-Steiner, M. Ch. Wide Band Gap p-Type Windows by CBD and SILAR Methods. *Thin Solid Films* **2004**, *451−452*, 128−132.

(30) Ni, Y.; Jin, Z.; Yu, K.; Fu, Y.; Liu, T.; Wang, T. Electrochemical Deposition Characteristics of p-CuSCN on n-ZnO Rod Arrays Films. *Electrochim. Acta* **2008**, *53*, 6048−6054.

(31) Wu, W.; Cui, S.; Yang, C.; Hu, G.; Wu, H. Electrochemically Superfilling of n-Type ZnO Nanorod Arrays with p-Type CuSCN Semiconductor. *Electrochem. Commun.* **2009**, *11*, 1736−1739.

(32) Zhang, Q.; Guo, H.; Feng, Z.; Lin, L.; Zhou, J.; Lin, Z. n-ZnO Nanorods/p-CuSCN Heterojunction Light-Emitting Diodes Fabricated by Electrochemical Method. *Electrochim. Acta* **2010**, *55*, 4889−4894.

(33) Hatch, S. M.; Briscoe, J.; Dunn, S. Improved CuSCN−ZnO Diode Performance with Spray Deposited CuSCN. *Thin Solid Films* **2013**, *531*, 404−407.

(34) Hatch, S. M.; Briscoe, J.; Sapelkin, A.; Gillin, W. P.; Gilchrist, J. B.; Ryan, M. P.; Heurtz, S.; Dunn, S. Influence of Anneal Atmosphere on ZnO-Nanorod Photoluminescent and Morphological Properties with Self-Powered Photodetector Performance. *J. Appl. Phys.* **2013**, *113*, 204501.

(35) Gertman, R.; Berger, Y.; Visoly-Fisher, I. Pulsed Electro-deposition of CuSCN for Superfilling of ZnO Nanowire Array Electrodes. *Electrochim. Acta* **2014**, *125*, 65−70.

(36) Pattanasattayavong, P.; Yaacobi-Gross, N.; Zhao, K.; Ndjawa, G.; Li, J.; Yan, F.; O'Regan, B. C.; Amassian, A.; Anthopoulos, T. D. Hole-Transporting Transistors and Circuits Based on the Transparent Inorganic Semiconductor Copper(I) Thiocyanate (CuSCN) Processed from Solution at Room Temperature. *Adv. Mater.* **2013**, *25*, 1504−1509.

(37) Hatch, S. M.; Briscoe, J.; Dunn, S. A Self-Powered ZnO-Nanorod/CuSCN UV Photodetector Exhibiting Rapid Response. *Adv. Mater.* **2013**, *25*, 867−871.

(38) Peng, L.; Hu, L.; Fang, X. Energy Harvesting for Nanostructured Self-Powered Photodetectors. *Adv. Funct. Mater.* **2014**, *24*, 2591−2610.

(39) Liu, K.; Sakurai, M.; Aono, M. ZnO-Based Ultraviolet Photodetectors. *Sensors* **2010**, *10*, 8604−8634.

(40) Soci, C.; Zhang, A.; Xiang, B.; Dayeh, S. A.; Aplin, D. P. R.; Park, J.; Bao, X. Y.; Lo, Y. H.; Wang, D. ZnO Nanowire UV Photodetectors with High Internal Gain. *Nano Lett.* **2007**, *7*, 1003−1009.

(41) Tsai, D. S.; Lin, C. A.; Lien, W. C.; Chang, H. C.; Wang, Y. L.; He, J. H. Ultra-High-Responsivity Broadband Detection of Si Metal-Semiconductor-Metal Schottky Photodetectors Improved by ZnO Nanorod Arrays. *ACS Nano* **2011**, *5*, 7748−7753.

(42) Nie, B.; Hu, J. G.; Luo, L. B.; Xie, C.; Zeng, L. H.; Lv, P.; Li, F. Z.; Jie, J. S.; Feng, M.; Wu, C. Y.; Yu, Y. Q.; Yu, S. H. Monolayer Graphene Film on ZnO Nanorod Array for High-Performance Schottky Junction Ultraviolet Photodetectors. *Small* **2013**, *9*, 2872–2879.

(43) Ni, P.; Shan, C.; Wang, S.; Liu, X.; Shen, D. Self-Powered Spectrum-Selective Photodetectors Fabricated from n-ZnO/p-NiO Core–Shell Nanowire Arrays. *J. Mater. Chem. C* **2013**, *1*, 4445.

(44) Li, X.; Gao, C.; Duan, H.; Lu, B.; Pan, X.; Xie, E. Nanocrystalline TiO$_2$ Film Based Photoelectrochemical Cell as Self-Powered UV-Photodetector. *Nano Energy* **2012**, *1*, 640–645.

(45) Gao, C.; Li, X.; Wang, Y.; Chen, L.; Pan, X.; Zhang, Z.; Xie, E. Titanium Dioxide Coated Zinc Oxide Nanostrawberry Aggregates for Dye-Sensitized Solar Cell and Self-Powered UV-Photodetector. *J. Power Sources* **2013**, *239*, 458–465.

(46) Bai, Z.; Yan, X.; Chen, X.; Liu, H.; Shen, Y.; Zhang, Y. ZnO Nanowire Array Ultraviolet Photodetectors with Self-Powered Properties. *Current Appl. Phys.* **2013**, *13*, 165–169.

(47) Consonni, V.; Rey, G.; Roussel, H.; Doisneau, B.; Blanquet, E.; Bellet, D. Preferential Orientation of Fluorine-Doped SnO$_2$ Thin Films: The Effects of Growth Temperature. *Acta Mater.* **2013**, *61*, 22–31.

(48) Harris, G. B. Quantitative Measurement of Preferred Orientation in Rolled Uranium Bars. *Philos. Mag.* **1952**, *43*, 113–123.

(49) Marí, B.; Singh, K. C.; Ortiz, L.; Mollar, M. Electrochemical Fabrication and Characterization of p-CuSCN/n-ZnO Heterojunction Devices. *J. Solid State Electrochem.* **2013**, *17*, 667–673.

(50) Kabesova, M.; Dunaj-Jurco, M.; Serator, M.; Gazo, J.; Garaj, J. The Crystal Structure of Copper(I) Thiocyanate and its Relation to the Crystal Structure of Copper(II) Diammine Dithiocyanate Complex. *Inorg. Chim. Acta* **1976**, *17*, 161–165.

(51) Smith, D. L.; Saunders, V. I. Preparation and Structure Refinement of the 2H Polytype of β-Copper(I) Thiocyanate. *Acta Crystallogr. B* **1982**, *38*, 907–909.

(52) Smith, D. L.; Saunders, V. I. The Structure and Polytypism of the β Modification of Copper(I) Thiocyanate. *Acta Crystallogr. B* **1981**, *37*, 1807–1812.

(53) Liu, C.; Wu, W.; Liu, K.; Li, M.; Hu, G.; Xu, H. Orientation Growth and Electrical Property of CuSCN Films Associated with the Surface States. *CrystEngComm* **2012**, *14*, 6750–6754.

(54) Hatch, S. M.; Briscoe, J.; Dunn, S. Improved CuSCN–ZnO Diode Performance with Spray Deposited CuSCN. *Thin Solid Films* **2013**, *531*, 404–407.

(55) O'Regan, B. C.; Lenzmann, F. Charge Transport and Recombination in a Nanoscale Interpenetrating Network of n-Type and p-Type Semiconductors: Transient Photocurrent and Photovoltage Studies of TiO$_2$/Dye/CuSCN Photovoltaic Cells. *J. Phys. Chem. B* **2004**, *108*, 4342–4350.

(56) O'Regan, B.; Lenzmann, F.; Muis, R.; Wienke, J. A Solid-State Dye-Sensitized Solar Cell Fabricated with Pressure-Treated P25–TiO$_2$ and CuSCN: Analysis of Pore Filling and IV Characteristics. *Chem. Mater.* **2002**, *14*, 5023–5029.

(57) Son, Y.; Tacconi, N. R.; Rajeshwar, K. Photoelectrochemistry and Raman Spectroelectrochemistry of Cuprous Thiocyanate Films on Copper Electrodes in Acidic Media. *J. Electroanal. Chem.* **1993**, *345*, 135–146.

(58) Sun, L.; Huang, Y.; Hossain, M. A.; Li, K.; Adams, S.; Wang, Q. Fabrication of TiO$_2$/CuSCN Bulk Heterojunctions by Profile-Controlled Electrodeposition. *J. Electrochem. Soc.* **2012**, *159*, D323–D327.

(59) Sirkar, S. J.; Bisrnu, B. L. On the Raman Spectra of a few Alkyl Sulphides in the Solid State. *Indian Natl. Sci. Acad. J.* **1943**, *9*, 287–293.

(60) Hamilton, J. C.; Farmer, J. C.; Anderson, R. J. In Situ Raman Spectroscopy of Anodic Films Formed on Copper and Silver in Sodium Hydroxide Solution. *J. Electrochem. Soc.* **1986**, *133*, 739–745.

(61) Zheng, Y. T.; Xuan, F. Z.; Wang, Z. In Situ Raman Monitoring of Stress Evaluation and Reaction in Cu$_2$O Oxide Layer. *Mater. Lett.* **2012**, *78*, 11–13.

(62) Minceva-Sukarova, B.; Najdoski, M.; Grozdanov, I.; Chunnilall, C. J. Raman Spectra of Thin Solid Films of Some Metal Sulfides. *J. Mol. Struct.* **1997**, *410–411*, 267–270.

(63) Ferrari, A. C.; Rodil, S. E.; Robertson, J. Interpretation of Infrared and Raman Spectra of Amorphous Carbon Nitrides. *Phys. Rev. B* **2003**, *67*, 155306.

(64) Maruska, H. P.; Namavar, F.; Kalkhoran, N. M. Current Injection Mechanism for Porous-Silicon Transparent Surface Light-Emitting Diodes. *Appl. Phys. Lett.* **1992**, *61*, 1338–1340.

(65) Minami, T.; Miyata, T.; Yamamoto, T. Work Function of Transparent Conducting Multicomponent Oxide Thin Films Prepared by Magnetron Sputtering. *Surf. Coat. Technol.* **1998**, *108–109*, 583–587.